JOURNAL OF GEOPHYSICAL RESEARCH, VOL. ???, XXXX, DOI:10.1029/,

The influence of meso-scale eddies on the soft-tissue carbon pump

Anne Willem Omta and Bas Kooijman

Department of Theoretical Life Sciences, Institute for Molecular Cell Biology, Faculty of Earth and Life Sciences, Vrije Universiteit, De Boelelaan 1081, 1081 HV Amsterdam, The Netherlands

Henk Dijkstra

Institute for Marine and Atmospheric Research Utrecht (IMAU), Department of Physics and Astronomy, Universiteit Utrecht, Princetonplein 5, 3582 CC Utrecht, The Netherlands

---

A.W.Omta, Department of Theoretical Life Sciences, Institute for Molecular Cell Biology, Faculty of Earth and Life Sciences, Vrije Universiteit, De Boelelaan 1081, 1081 HV Amsterdam, The Netherlands. (anne.willem.omta@falw.vu.nl)

Abstract. In an idealized situation of a baroclinically unstable single eddy, we study the impact of the eddy induced mixing on the soft-tissue carbon pump. The new element here is the use of a three-dimensional nonhydrostatic ocean model coupled to a physiological plankton model that is able to represent a flexible plankton stoichiometry and hence a variable Redfield ratio. During the development and breakup of the eddy, a complicated plankton pattern appears. The processes of plankton growth and transport and the net effect on the Redfield ratio are studied in detail. Our main result is that the physical processes associated with eddy breakup lower the Redfield ratio and hence weaken the soft-tissue carbon pump.

1. Introduction

The marine biosphere is an important component in the global carbon cycle. Here the ocean circulation with all its variability interacts with marine life and its associated chemistry. One of the central processes is the biological carbon pump which involves gas exchange between the ocean and atmosphere, plankton dynamics and ocean mixing. As the atmospheric carbon dioxide concentration is dependent on the strength of the biological carbon pump, it is crucial to understand its precise details.

The soft-tissue carbon pump was first defined by *Volk and Hoffert* [1985] as the difference in carbon dioxide concentration between the surface and the deep ocean caused by the growth, sinking, and remineralisation of algae. This difference is determined by the nutrient utilisation and the stoichiometry of the sinking organic material according to *Broecker* [1982]

$$\Delta C = R\Delta N \tag{1}$$

Here, ΔC is the difference in inorganic carbon concentration between the surface and the deep sea, R the C:N (Redfield) ratio of the sinking organic material, and ΔN the difference in inorganic nitrogen concentration between the surface and the deep ocean. The relationship (1) follows from the assumption of a dynamic equilibrium between the sinking of organic material and the up-

ward diffusion of inorganic carbon and nutrients. Although it has been known for a long time that the chemical composition of algae is highly variable *Droop* [1974], biogeochemists have assumed a constant oceanic Redfield ratio until recently. However, during the last 15 years, wide-spread deviations from the classical Redfield C:N:P ratios have been observed in the ocean *Sambrotto et al.* [1993]; *Emerson et al.* [2001]; *Karl et al.* [2002].

Plankton stoichiometry as well as productivity is usually determined by the availability of limiting nutrients (such as nitrate and phosphate) which are mainly supplied from the deep waters through vertical transport *Orcutt et al.* [2001]; *Zehr and Ward* [2002]. Strong vertical motions occur in mesoscale ocean flows (i.e., those associated with spatial scales of the order of 10-100 km). Eddies, fronts and filaments therefore substantially affect marine ecosystems as well as biogeochemical fluxes *McGillicuddy et al.* [1998]; *Oschlies and Garçon* [1998]; *Martin and Richards* [2001]. In recent years, numerical simulations of primary production have been performed with horizontal resolutions able to adequately capture mesoscale variability. In *Lévy et al.* [2001]; *Lévy* [2003], eddies were generated from an unstable zonal baroclinic jet and resulting horizontal and vertical distributions of phytoplankton were studied. The results showed a strong correlation between vorticity and new production and stressed the

importance of vertical transports at the mesoscale on the plankton distributions. It is therefore unfortunate that many coupled physical-biological models for the carbon pump do not resolve mesoscale ocean flows *Sarmiento et al.* [1998]; *Heinze* [2002]; *Aumont et al.* [2003].

Using a mixed layer model coupled to a physiological plankton model allowing for flexible plankton stoichiometry, *Omta et al.* [2006] have shown that external flow properties, such as mixed layer processes, can affect the Redfield ratio and hence the soft-tissue carbon pump. In the light-limited regime, the C:N ratio decreases with increasing temperature and hence provides a positive feedback between temperature and atmospheric CO_2 (through variations in plankton stoichiometry). This feedback may be important to explain changes in atmospheric CO_2 during glacial-interglacial transitions.

As mesoscale flows are central in the vertical transport of nutrients, an important issue is to study the effect of these mesoscale features on the soft-tissue carbon pump through flexible plankton stoichiometry. To understand these effects in quite detail, we have chosen here a relatively simple mesoscale flow situation of a single geostrophic eddy which is baroclinically unstable. The advantage of this flow over a field of transient eddies

as in *Lévy et al.* [2001] is that the transient vertical velocity field has a relatively simple spatial structure.

In section 2, the hydrodynamic and biological model as well as details of the numerical implementation of the coupled model are presented. Results on the flow patterns and the plankton and nutrient distributions for a reference simulation are presented in section 3 and further analyzed in section 4. Our main result is that the flow induced by the baroclinically unstable mesoscale eddy leads to a lower nutrient utilization and to a lower C:N ratio. The implications of this result are discussed in the last section of the paper.

2. Models and Methods

We consider a horizontally square domain of length $L = 32$ km with a constant depth H of 1 km. This flow domain is situated on a midlatitude f plane with a constant Coriolis parameter $f_0 = 10^{-4}$ s^{-1}. To simulate the flows in this domain, we use the nonhydrostatic three-dimensional hydrodynamic model as described in section 2.2 below. The flow transports nutrients and biomass according to a plankton model that includes flexible stoichiometry. The biological model is presented in section 2.1 and the numerical implementation of the coupled physical-biological model and the choice of initial conditions are described in section 2.3.

2.1. The biological model

Because the strength of the soft-tissue carbon pump is determined by the stoichiometry of the organic material sinking into the deep sea, we consider flexible stoichiometry as a necessary element of any biological model that is applied for modelling the biological carbon pump. The primary mechanism known to cause variations in stoichiometry is found at the base of the foodweb: phytoplankton engages in luxury consumption, storing excess photosynthate (as starch or lipids) and nutrients (e.g. nitrate, phosphate) internally. This storage is particularly notable under limitation: nutrient-limited phytoplankton stores high amounts of photosynthate-derivates, whereas light-limited phytoplankton can build up high nutrient concentrations in vacuoles. Individual uptake and storage mechanisms are thus obviously decoupled. As a result, the stoichiometry of phytoplankton is by no means limited to the classical Redfield ratio: due to luxury consumption it can be highly variable.

Inspired by the one-reserve mixotroph model described by *Kooijman et al.* [2002], we have developed a model which is able to represent flexible stoichiometry. This Phytoplankton Internal Nitrogen and Carbon (PINC) model is again based on the Dynamic Energy Budget (DEB) theory proposed by *Kooijman* [2000]. The DEB theory offers a modelling framework for

individuals and populations with their stoichiometries based on first principles. Cornerstone of the theory is the partitioning of total biomass into structural mass and one or more reserves. We apply this principle to distinguish three components with different elemental compositions within the phytoplankton population: structural mass (consisting of carbon and nutrient in a fixed 10:1 ratio), an organic carbon reserve (consisting of carbon only), and a nitrogen reserve (consisting of nitrogen only). The ratios of these three components with respect to each other determine the carbon:nutrient ratio of the organisms.

The PINC model is schematically depicted in Fig. 1 and its governing equations and standard values of the parameters are presented in full detail in the Appendix. With these parameter values, the maximum growth rate is approximately 2 d^{-1}. Note that this growth rate can only be reached when both the nutrient concentration and the irradiance are high. A full description of the model is given in *Omta et al.* [2006]. In the model, a distinction is made between the carbon contribution to detritus (X_{DC}) and the nitrogen contribution (X_{DN}), and hence there are 7 state variables: dissolved inorganic carbon (X_C), dissolved inorganic nitrogen (X_N), structure volume (X_V), carbon reserve (X_{E_C}), nitrogen reserve (X_{E_N}), carbon detritus (X_{DC}) and nitrogen de-

Fig. 1

tritus (X_{DN}). We will label the variables in this sequence below as $X_i, i = 1, ...7$.

2.2. The hydrodynamic model

We make use of the nonhydrostatic flow model of *Molemaker and Dijkstra* [2000] to simulate the flow fields. The velocity field $\mathbf{u}$ and pressure field p are described by the three-dimensional Navier-Stokes equations and the continuity equation. The evolution of the temperature field T and the biological quantities is described by advection-diffusion equations. We assume a linear equation of state relating the density ρ to the temperature of the form $\rho = \rho_0(1 - \alpha(T - T_0))$ where $\rho_0 = 10^3$ kg m^{-3} and $T_0 = 15°$C are reference values and $\alpha = 10^{-5}$ K^{-1} is the constant expansion coefficient. Using the Boussinesq approximation, the governing equations are

$$\begin{aligned}
\frac{\partial \mathbf{u}}{\partial t} + (\mathbf{u}\cdot\nabla)\mathbf{u} \;+\; & f_0\mathbf{e_z}\times\mathbf{u} = -\frac{1}{\rho_0}\nabla p \\
&+\; \kappa_H(\frac{\partial^2}{\partial x^2} + \frac{\partial^2}{\partial y^2})\mathbf{u} + \kappa_V\frac{\partial^2\mathbf{u}}{\partial z^2} - \mathbf{e_z}\frac{g\rho}{\rho_0} \qquad (2)\\
\nabla\cdot\mathbf{u} \;=\; & 0 \qquad (3)\\
\frac{\partial T}{\partial t} + (\mathbf{u}\cdot\nabla)T \;=\; & \kappa_H(\frac{\partial^2}{\partial x^2} + \frac{\partial^2}{\partial y^2})T + \kappa_V\frac{\partial^2 T}{\partial z^2} \qquad (4)\\
\frac{\partial X_i}{\partial t} + (\mathbf{u}\cdot\nabla)X_i \;=\; & \kappa_H(\frac{\partial^2}{\partial x^2} + \frac{\partial^2}{\partial y^2})X_i + \kappa_V\frac{\partial^2 X_i}{\partial z^2} \\
&+\; F_i, i = 1, ..., 7 \qquad (5)
\end{aligned}$$

where $\mathbf{e_z}$ is the unit vector in the vertical direction and g is the gravitational acceleration. The fluxes F_i, i = 1, ..., 7 follow

from the PINC model and are defined in the Appendix. The quantities κ_H and κ_V are horizontal and vertical mixing coefficients of momentum and heat as in *Molemaker and Dijkstra* [2000]. Here, these are taken constant with values of $\kappa_H = 0.1$ $\mathrm{m^2 s^{-1}}$ and $\kappa_V = 1.0 \times 10^{-5}$ $\mathrm{m^2 s^{-1}}$. The latter value was chosen to obtain a vertical diffusion time scale H^2/κ_V on the order of thousand years in the deeper parts of the flow domain.

Let ΔT be a characteristic temperature difference between the top and bottom of the domain and X_i^0, i = 1, ..., 7, characteristic values of the biological quantities. When the equations are nondimensionalised using scales H, $\frac{\kappa_H}{H}$, $\frac{\rho_0 \kappa_H^2}{H^2}$ and $\frac{H^2}{\kappa_H}$, ΔT and X_i^0 for length, velocity, pressure, time, temperature, and biological quantities, respectively, three dimensionless parameters appear. These are the Rayleigh number Ra, the Taylor number Ta and the mixing ratio κ given by

$$Ra = \frac{H^3 g \alpha \Delta T}{\kappa_H^2}, Ta = \frac{H^4 f^2}{\kappa_H^2}, \kappa = \frac{\kappa_V}{\kappa_H}. \tag{6}$$

Standard values of these parameters are $Ra = 10^7 \Delta T$, $Ta = 2 \times 10^6$ and $\kappa = 10^4$.

The domain is assumed periodic in the horizontal and hence periodic boundary conditions are applied for all quantities. The top boundary is assumed to be stress free while the bottom boundary satisfies no-slip conditions. The top and bottom boundaries satisfy no-flux conditions for temperature. The

boundary conditions at the top ($z = 0$) and bottom ($z = -H$) are:

$$\frac{\partial X_i}{\partial z} = 0, i = 1, ..., 7; \frac{\partial T}{\partial z} = 0; \frac{\partial u}{\partial z} = 0; \frac{\partial v}{\partial z} = 0; w = 0 \qquad (7)$$

2.3. Numerical implementation and Initial Conditions

The governing non-hydrostatic equations are discretized in space using second-order central differences on an equidistant staggered grid. Together with the boundary conditions, the discretized equations form a closed set of (coupled) ordinary differential equations. For example, the momentum equations can be written as

$$\frac{\partial \mathbf{u}_{i,j,k}}{\partial t} = -\nabla \hat{p}_{i,j,k} + \mathbf{F}_{i,j,k}(\mathbf{u}, T) \qquad (8)$$

for $i = 1 \cdots N$, $j = 1 \cdots M$, $k = 1 \cdots L$ and $\hat{p} = p/\rho_0$. In our simulations, we use $N = M = 200$ and $L = 50$ providing a horizontal and vertical resolution of 160 m and 20 m, respectively. In (8), the $\mathbf{F}_{i,j,k}$ represent the (discretized) advective, diffusive and buoyancy terms. The set of equations (8) is integrated in time using an Adams-Bashforth method that is second order accurate in time, i.e.

$$\mathbf{u}^{n+1}_{i,j,k} = \mathbf{u}^{n}_{i,j,k} + \Delta t \left(\frac{3}{2}(\mathbf{F}^{n}_{i,j,k} - \nabla \hat{p}^{n}_{i,j,k}) - \frac{1}{2}(\mathbf{F}^{n-1}_{i,j,k} - \nabla \hat{p}^{n-1}_{i,j,k}) \right) \qquad (9)$$

where n indicates the time index. Taking the divergence of (9) gives

$$D_{i,j,k}^{n+1} = D_{i,j,k}^{n} + \Delta t \left(\frac{3}{2}(S_{i,j,k}^{n} - \nabla^2 p_{i,j,k}^{n}) - \frac{1}{2}(S_{i,j,k}^{n-1} - \nabla^2 p_{i,j,k}^{n-1}) \right) \tag{10}$$

where $D = \nabla \cdot \mathbf{u}$ and $S = \nabla \cdot \mathbf{F}$. The pressure acts in this case as a constraint which ensures that the flow will remain divergence-free. To solve for the pressure at every time step, (10) is rearranged and we demand $D_{i,j,k}^{n+1} = 0$. This leads to a Poisson equation

$$\nabla^2 \hat{p}_{i,j,k}^{n} = \frac{2}{3} D_{i,j,k}^{n} + \Delta t \left(S_{i,j,k}^{n} - \frac{1}{3}(S_{i,j,k}^{n-1} - \nabla^2 \hat{p}_{i,j,k}^{n-1}) \right) \tag{11}$$

At time n, all the terms of the right hand side of (11) are known so we can solve for $\hat{p}_{i,j,k}^{n}$ and hence for $\mathbf{u}_{i,j,k}^{n+1}$. Boundary conditions for the pressure at the upper and lower boundary are found using the momentum equations and realizing that $w = 0$ at $z = 0$ and $z = -H$.

The equations for the biological quantities require a more sophisticated advection scheme to prevent the occurrence of negative concentrations. We have used a third-order upwind scheme with limiter *Hundsdorfer and Verwer* [2003] for the advection of the biological tracers.

As the flow is neither forced at the surface nor in the internal part of the domain, the initial conditions are central for the evolution of the flow field and biological fields. To define an ini-

tial eddy flow field, we first choose the background temperature stratification as *Molemaker and Dijkstra* [2000]

$$T_b(z) = \Delta T(T_0 + T_1 e^{\gamma z}) \tag{12}$$

where γ is a measure for the vertical temperature decay. Next, we superpose a temperature field on this background defined by

$$T_e(r,z) = \Delta T A_e e^{-\alpha_e r^6} e^{\gamma_e z} \tag{13}$$

where $r = ((x - L/2)^2 + (y - L/2)^2)^{1/2}$ is the distance from the centre of the domain, A_e is a typical amplitude, α_e controls the horizontal decay scale, and γ_e defines the vertical decay scale.

The initial flow velocity field is assumed to be in cyclo-geostrophic equilibrium with the total initial temperature field $T_b + T_e$. This initial velocity field is given by

$$u = 0; v = \frac{rf_0}{2}(\sqrt{1 - \frac{4\alpha g}{rf_0^2}\int_{-H}^{z} \frac{\partial T_e}{\partial r} dz'} - 1); w = 0 \tag{14}$$

with u the radial velocity, v the azimuthal velocity, and w the vertical velocity. In the results below, we have chosen $\Delta T =$ 10K, $\gamma H = 2.4, \gamma_e H = 4.0$, $A_e/\Delta T = 0.6$ and $\alpha_e H^6 = 0.0004$. For these values, the initial horizontal velocity field is plotted in Fig. 2. A typical radius of the eddy is given by $r = (1/\alpha_e)^{1/6} \approx$ 4.0 km and hence the eddy diameter is about 8 km in accordance with Fig. 2. Maximum horizontal velocities are about 0.1 ms^{-1}.

Fig. 2

The initial conditions for the biological fields were determined by a simulation of the PINC model under motionless and hori-

zontally homogeneous conditions. We took the vertical diffusion $\kappa_V = 1.0 \times 10^{-5} m^2 s^{-1}$ everywhere in the domain. The simulation was run, until an equlibrium between sinking of organic detritus and inorganic carbon and nitrogen had been approached.

3. Results

From the initial conditions, the model was integrated in time over a time interval of about 12 days. The perturbations associated with baroclinic instability rapidly grow in time. Although the instability starts at the edge of the eddy, it leads to high vertical velocities in the center of the eddy after 4 days (Fig. 3). The Eady timescale is approximately 0.7 days which is of the same order of magnitude as the biological timescale. Note that in contrast to the geostrophic eddy in *Molemaker and Dijkstra* [2000] the initial eddy is unstable without surface cooling, because of the larger horizontal gradients in the density structure (an r^6 dependence instead of an r^2 dependence). After day 4, the flow becomes irregular due to the break up of the eddy into substructures.

Fig. 3

3.1. Temporal-spatial structures

Just as in *Molemaker and Dijkstra* [2000], an azimuthal wavenumber $m = 4$ pattern, the most unstable eigenmode, grows in time and the anomalies rotate counterclockwise (with

an angular velocity of about 30 cm s^{-1}) around the eddy. The spatial patterns of the vertical velocity w, the nutrient distribution X_N and the structural volume distribution X_V at day 3.6 are plotted in Fig. 4. After 3.6 days, the four-lobe pattern is already developed and the maximum and minimum vertical velocities are strongly localized near the end of each lobe (Fig. 4a). Newly upwelled water has a low biomass concentration but a high nutrient concentration. The distribution pattern of X_N (Fig. 4b) therefore has highest positive values (the white regions) at the locations of maximum upwelling in Fig. 4a. In those areas, the biomass concentration is relatively low (Fig. 4c).

Fig. 4

Because of the high nutrient concentration in the upwelling regions, the algae can grow at maximum rate and after a few days, the upwelled water has a high biomass concentration (Fig. 5). The distribution of biomass after 7.2 days (Fig. 5c) shows a bit more fine structure than the nutrient distribution (Fig. 5b). Each of the lobes shows an asymmetric dipolar structure and within the eddy center and the lobes, there is a lot of vertical mixing (Fig. 5a). The nutrient concentration is high everywhere and also the biomass concentration is relatively high in most places. However, within the region of high vertical mixing, biomass concentrations are low at sites where there has been recent upwelling or where upwelling still takes place because the

Fig. 5

biota have not yet had the time to grow. As can be seen from Fig. 5a and c, the places with low biomass concentrations within the lobes are actually upwelling sites.

After 12 days, the lobes have moved nearly to the boundary of the domain (Fig. 6). The inner eddy appears to undergo again an instability associated with an $m = 4$ mode, while the lobes seem to become unstable to an $m = 2$ mode (Fig. 6a). The $m = 4$ spatial structure can be seen in the inner eddy nutrient concentration (Fig. 6b) but the amplitudes in the lobes are too weak to see the $m = 2$ structure. The upwelling is now very localized but the biomass is still increasing at locations of earlier upwelling. Every water mass that has experienced upwelling more than a few days ago has a high biomass concentration. Hence, the structural mass concentrations are high in a large region around the eddy centre; the highest concentrations are found along the tracks of the centers of the lobes (Fig. 6c).

Fig. 6

3.2. Redfield ratio

Using the results of the simulation described in the previous subsection, we computed horizontally averaged quantities and from this the C:N ratio of the organic material. As the strength of the soft-tissue carbon pump is determined by both the nutrient utilisation ΔN and the C:N (Redfield) ratio of the organic

material, we are interested in the effect of the eddy on those two features.

The initial C:N ratio (computed from a solution with no flow) is relatively large near the surface (Fig. 7a). Over the following 7 days, the overall values decrease and more rapidly near the surface. This decrease of the C:N ratio can be explained, if one considers the vertical mixing induced by the eddy. Higher vertical mixing leads to a higher supply of nitrate but at the same time the plankton is mixed to greater depths, where there is less light. This, in turn, leads to an enhanced uptake of nitrogen and a reduced uptake of carbon, leading to a higher nitrogen reserve concentration and a lower carbon reserve concentration, and hence a lower C:N ratio. This general effect of mixing on the composition of organic matter is described in more detail in *Omta et al.* [2006]. At later times, the net effect of the mixing on the C:N ratio decreases since the amplitudes of the vertical velocities have decreased and hence the C:N ratio increases again near the surface.

Fig. 7

During the entire period of our simulation, the algal population is still too small to consume the new nutrients that the eddy circulation brings into the euphotic zone, leading to a slightly higher surface nutrient concentration (Fig. 7b; the effect is so small that it is almost invisible) and hence a lower nutrient util-

isation and a net growth of the population (Fig. 7c). This net growth will proceed, until the surface nutrient concentration is such that the primary production rate cancels against the death rate (which was also the case at the start of the simulation). However, even when this equilibrium has been achieved, the average surface nutrient concentration should be different from that at the start of the simulation. We will address this issue in more detail in the analysis section below.

In summary, both the lower nutrient utilization and the eddy stirring lead to a weakening of the biological soft-tissue carbon pump. We have varied the eddy size while keeping other parameters constant and the magnitudes of these effects remained approximately the same, as long as the eddy was baroclinically unstable.

4. Analysis

As we have seen above, the biological carbon pump is not only weakened by a change in the plankton stoichiometry, but also by a slightly lower nutrient utilisation. In our simulations, this effect is very weak, but in situations with more vigorous vertical velocities, e.g. in frontal regions, it may be very important. Furthermore, it appears to be quite a general effect. Throughout the remainder of this section, we will demonstrate that, under reasonable assumptions, the nutrient utilisation will always be

lower if the nutrient distribution is inhomogeneous than if the nutrient distribution is homogeneous.

The assumptions that need to be made are the following:

1) The direct effect of grazing on the phytoplankton population size can be neglected (as we have actually done in our model).

2) The growth rate of the plankton ($\dot{j}_{V,G}$) equals the uptake rate of the limiting nutrient ($\dot{j}_{E_N,A_m}$) minus the maintenance rate ($\dot{k}_M$).

3) Vertical advection and diffusion of phytoplankton itself (i.e. not of nutrients) can be neglected.

4) The growth rate and the biomass concentration are spatially uncorrelated, i.e. $< \dot{j}_{E_N,A} X_V >=< \dot{j}_{E_N,A} >< X_V >$ (which means roughly that the nutrient and biomass distributions are spatially uncorrelated).

We can check assumption 4) in our simulations and the results in Fig. 8 indeed provide support. The nutrient distribution and the biomass distribution are practically uncorrelated, because the organisms need time to grow. At an upwelling site, nutrient-rich and biomass-poor water is advected upward. In time, nutrients are converted into a higher biomass concentration, but during this process, upwelling starts at other locations,

Fig. 8

providing new nutrient-rich and biomass-poor water to the surface.

The time evolution of the structural biomass is given by (from (5) and the Appendix)

$$\begin{aligned}\frac{\partial X_V}{\partial t} &= X_V(\dot{j}_{V,G} - \dot{j}_{V,H}) + \kappa_H(\frac{\partial^2}{\partial x^2} + \frac{\partial^2}{\partial y^2})X_V \\ &+ \kappa_V \frac{\partial^2 X_V}{\partial z^2} - (\mathbf{u}\cdot\nabla)X_V \end{aligned} \quad (15)$$

Neglecting advection and diffusion of the phytoplankton, this equation reduces to

$$\frac{\partial X_V}{\partial t} = X_V(\dot{j}_{V,G} - \dot{j}_{V,H}) \quad (16)$$

Furthermore, with assumption 2), the uptake rate $\dot{j}_{E_N,A}$ is equal to:

$$\begin{aligned}\dot{j}_{E_N,A} &= \dot{j}_{E_N,Am}\frac{X_N}{X_N+K_N} = \dot{j}_{E_N,Am}(\frac{X_N+K_N}{X_N+K_N} - \frac{K_N}{X_N+K_N}) \\ &= \dot{j}_{E_N,Am}(1 - \frac{K_N}{X_N+K_N}) \end{aligned} \quad (17)$$

and hence we find

$$\dot{j}_{V,G} = \dot{j}_{E_N,Am}\left(1 - \frac{K_N}{X_N+K_N}\right) - \dot{k}_M \quad (18)$$

At equilibrium ($\partial X_V/\partial t = 0$) we have either $X_V = 0$ (which means that all the organisms have gone extinct) or:

$$\dot{j}_{V,H} = \dot{j}_{V,G} = \dot{j}_{E_N,Am}\left(1 - \frac{K_N}{X_N+K_N}\right) - \dot{k}_M \quad (19)$$

Rearranging the terms we get

$$X_N \equiv X_N^H = \frac{K_N}{1 - \frac{\dot{j}_{V,H}+\dot{k}_M}{\dot{j}_{E_N,Am}}} - K_N \quad (20)$$

An algal population in the irregular environment of a geophysical flow, however, never reaches such an equilibrium at specific points within the domain. In this case, we can eliminate the small-scale variability by taking the average over a relatively large area. Such a horizontally averaged value of X_V will at some point reach a statistical equilibrium $< X_V >$ as a solution of (using the periodic boundary conditions)

$$\frac{\partial < X_V >}{\partial t} = < \dot{j}_{V,G} X_V > - < \dot{j}_{V,H} X_V > + < \kappa_V \frac{\partial^2 X_V}{\partial z^2} > - < w \frac{\partial X_V}{\partial z} >= 0 \quad (21)$$

With assumption 3), $\frac{\partial < X_V >}{\partial t} = 0$ means that $< \dot{j}_{V,H} X_V >=< \dot{j}_{V,G} X_V >$. With assumption 4), and considering that $\dot{j}_{V,H}$, k_M, and $\dot{j}_{E_N,Am}$ are constants, we obtain the following equation analogous to (19):

$$\dot{j}_{V,H} + \dot{k}_M = \dot{j}_{E_N,Am}(1 - < \frac{K_N}{X_N + K_N} >) \quad (22)$$

which means that

$$< \frac{K_N}{X_N + K_N} >= 1 - \frac{\dot{j}_{V,H} + \dot{k}_M}{\dot{j}_{E_N,Am}} \quad (23)$$

From the Chebyshev integral inequality *Mitrinovic* [1970] it can be shown that:

$$\frac{K_N}{< X_N > + K_N} \leq < \frac{K_N}{X_N + K_N} > \quad (24)$$

(the left- and righthandside are equal, if the nutrient distribution is homogeneous) and combining this with (23) yields:

$$\frac{K_N}{< X_N > + K_N} \leq 1 - \frac{\dot{j}_{V,H} + \dot{k}_M}{\dot{j}_{E_N,Am}} \tag{25}$$

and hence

$$< X_N > \geq \frac{K_N}{1 - \frac{\dot{j}_{V,H} + \dot{k}_M}{\dot{j}_{E_N,Am}}} - K_N = X_N^H \tag{26}$$

The equality indeed holds if the nutrient distribution is homogeneous, so the average nutrient concentration is always higher if the nutrient distribution is inhomogeneous than if the nutrient distribution is homogeneous.

5. Discussion and conclusions

We have simulated a phytoplankton population within a mesoscale eddy. Within this eddy, baroclinic instability caused a vertical circulation pattern, bringing nutrient-rich and biomass-poor water to the surface. The interplay between upwelling and biological uptake leads to a fine structure in the biomass distribution: upwelling regions are biomass-poor, while water that has upwelled more than a week ago is rich in biomass.

An interesting feature is the effect of upwelling on the biomass concentration and distribution. Upwelling brings water with a high nutrient and a low biomass concentration to the surface and hence newly upwelled water has a low biomass concentration. In this newly upwelled water, algae grow at maximum speed

because of the high nutrient concentration, and therefore oldly upwelled water, i.e. water that has upwelled more than a few days ago, has a relatively high biomass concentration. This time delay leads to a fine structure in the biomass concentration, an effect similar to what was described by *Abraham* [1998] who modelled phytoplankton and zooplankton in a chaotic flow. The phytoplankton patterns were similar to the flow patterns, but the zooplankton patterns showed marked fine structure, because *Abraham* [1998] included a maturation time in the zooplankton dynamics, i.e. there was a time delay between the consumption of phytoplankton and the birth of new zooplankton.

Compared to *Lévy et al.* [2001]; *Lévy* [2003], we have simulated plankton growth in a relatively simple flow and hence we were able to analyse the plankton distribution patterns in more detail. This detailed analysis led to somewhat different conclusions regarding at which sites high biomass concentrations can be found. According to *Lévy et al.* [2001]; *Lévy* [2003], biomass and primary productivity are high in regions with strong frontal dynamics, i.e. regions with vertical transports, whereas our analysis reveals that primary productivity and biomass concentrations are often low in regions with strong vertical mixing. In those regions, nutrient-rich and biomass-poor water is brought to the surface. Only when this water has been at the surface

for about one week, there has been enough time to convert the high nutrient concentration into a high biomass concentration. Our results are different from *Lévy et al.* [2001]; *Lévy* [2003], because the radii of their eddies were approximately 10 times as large as the radii of our eddies. Because the growth rate was approximately the same in *Lévy et al.* [2001]; *Lévy* [2003], their ratio of the biological timescale to the advective timescale was much smaller than ours.

The eddy-induced flow led to a decrease of the C:N ratio of the plankton and to a lower nutrient utilisation which should both lead to a weakening of the biological carbon pump. The effect on the C:N ratio was caused by the same biological mechanism as the effect of mixed-layer on the C:N ratio *Omta et al.* [2006]. The lower nutrient utilisation was shown in section 4 to be due to the inhomogeneous nutrient distribution caused by the presence of the eddy. We have derived this result while neglecting vertical diffusion and advection of the plankton. This is, of course, highly unrealistic since the inhomogeneous nutrient distributions are generated by advection. Vertical diffusion does give a net downward transport of biomass from the surface into the deep. However, the loss rate should be approximately the same in the homogeneous and inhomogeneous cases, because it scales as κ_V/H_{eu}^2 (with H_{eu} the depth of the euphotic

zone in which the algae grow) and κ_V and H_{eu} are constant in this model. Vertical advection will yield an extra net loss of biomass from the surface layer, because all vertical water movements tend to diminish the surface biomass concentration. Upwelling brings deep water without biomass to the surface while downwelling does not bring any biomass to the surface: it only transports biomass from the surface into the deep. This means that the average growth rate $< \dot{j}_{V,G} >$ must be higher in the inhomogeneous case to compensate for this extra loss. This is an additional reason why the average nutrient concentration should be higher in the inhomogeneous case than in the homogeneous case.

Although the simulations provide a clear qualitative picture of the impact of the eddy on nutrient utilisation and the C:N ratio, the effect on the nutrient utilisation is very small and it is difficult to provide a reliable quantitative estimate of the effect of the eddy on the C:N ratio. Furthermore, it is not clear whether variations in the stoichiometry of the phytoplankton growing at the surface of the ocean translate into variations in the stoichiometry of the sinking organic material. In fact, the composition of the sinking material seems to be pretty constant across the world ocean *Schneider et al.* [2003], while large variations in the stoichiometry of the consumption of carbon, nitrogen, and phos-

phorus by phytoplankton have been observed at the surface of the ocean (e.g. *Sambrotto et al.* [1993]; *Arrigo et al.* [1999]). This could suggest that the sinking organic material is very rich in one compound and that all the other organic compounds are largely remineralised within the euphotic zone. From this viewpoint, it is interesting that the C:N ratio of the sinking organic matter is on average very close to the C:N ratio of chitin (i.e. 8) and it is unfortunate that the composition of POM is usually only given in terms of elements and not in terms of chemical compounds. It is not known whether the observations of overconsumption of carbon were performed within eddies. In fact, there have not yet been any systematic observational studies of the effect of eddies on plankton stoichiometry, as far as we know. We hope that our simulation results will stimulate such studies in the near future.

Acknowledgments.

We would like to thank Jorn Bruggeman and Bob Kooi for their careful reading of the manuscript and for their helpful comments. This work was financially supported through the Computational Life Science program of the Netherlands Organisation for Scientific Research (NWO) under Grant No. 635.100.009.

References

Abraham, E. R. (1998), The generation of plankton patchiness by turbulent stirring, *Nature*, *391*, 577–580.

Arrigo, K., D. Robinson, D. Worthen, R. Dunbar, G. DiTullio, M. Vanwoert, and M. Lizotte (1999), Phytoplankton community structure and the drawdown of nutrients and co_2 in the southern ocean, *Science*, *283*, 365–367.

Aumont, O., E. Maier-Reimer, S. Blain, and P. Monfray (2003), An ecosystem model of the global ocean including fe, si, p colimitations, *Global Biogeochemical Cycles*, *17*, 29.

Broecker, W. S. (1982), Ocean geochemistry during glacial time, *Geochimica et Cosmochimica Acta*, *46*, 1689–1705.

Droop, M. R. (1974), The nutrient status of algal cells in continuous culture, *J. Mar. Biol. Ass. UK*, *54*, 825–855.

Emerson, S., S. Mecking, and J. Abell (2001), The biological pump in the subtropical north pacific ocean: Nutrient sources, redfield ratios, and recent changes, *Global Biogeochemical Cycles*, *15*, 535–554.

Heinze, C. (2002), Assessing the importance of the southern ocean for natural atmospheric pco_2 variations with a global biogeochemical general circulation model, *Deep-Sea Research II*, *49*, 3105–3125.

Hundsdorfer, W., and J. G. Verwer (2003), *Numerical Solution of Time-Dependent Advection-Diffusion-Reaction Equations*, 1st ed., Springer Verlag, Berlin.

Karl, D. M., K. M. Björkman, J. E. Dore, L. Fujieki, D. V. Hebel, T. Houlihan, R. M. Letelier, and L. M. Tupas (2002), Ecological nitrogen-to-phosphorus stoichiometry at station aloha, *Deep-Sea Research II*, *29*, 2074.

Kooijman, S. A. L. M. (2000), *Dynamic energy and mass budgets in biological systems*, Cambridge University Press, Cambridge.

Kooijman, S. A. L. M., H. A. Dijkstra, and B. W. Kooi (2002), Light–induced mass turnover in a mono–species community of mixotrophs, *Journal of Theoretical Biology*, *214*, 233–254.

Lévy, M. (2003), Mesoscale variability of phytoplankton and of new production: Impact of the large-scale nutrient distribution, *Journal of Geophysical Research*, *108*, 22.

Lévy, M., P. Klein, and A. M. Treguier (2001), Impacts of submesoscale physics on phytoplankton production and subduction, *Journal of Marine Research*, *59*, 535–565.

Martin, A. P., and K. J. Richards (2001), Mechanisms for vertical nutrient transport within a north atlantic mesoscale eddy, *Deep-Sea Res. II*, *48*, 757–773.

McGillicuddy, D. J., A. R. Robinson, D. A. Siegel, H. W. Jannasch, R. Johnson, T. D. Dickey, J. McNeil, A. F. Michaels,

and A. H. Knap (1998), Influence of mesoscale eddies on new production in the sargasso sea, *Nature*, *394*, 263–266.

Mitrinovic, D. S. (1970), *Analytic inequalities*, Springer, Berlin.

Molemaker, M. J., and H. A. Dijkstra (2000), Stability of a cold–core eddy in the presence of convection: hydrostatic versus nonhydrostatic modeling, *Journal of Physical Oceanography*, *30*, 475–494.

Omta, A. W., J. Bruggeman, S. A. L. M. Kooijman, and H. A. Dijkstra (2006), The biological carbon pump revisited: feedback mechanisms between climate and the redfield ratio, *Geophysical Research Letters*, *accepted for publication*.

Orcutt, K. M., F. Lipschultz, K. Gundersen, R. Arimoto, A. F. Michaels, A. H. Knap, and J. R. Gallon (2001), A seasonal study of the significance of nitrogen fixation by trichodesmium spp. at the bermuda atlantic time-series study (bats) site, *Deep–Sea research II*, *48*, 1583–1608.

Oschlies, A., and V. Garçon (1998), Eddy–induced enhancement of primary production in a model of the north atlantic ocean, *Nature*, *394*, 266–269.

Sambrotto, R. N., et al. (1993), Elevated consumption of carbon relative to nitrogen in the surface ocean, *Nature*, *363*, 248–250.

Sarmiento, J. L., T. M. C. Hughes, R. J. Stouffer, and S. Manabe (1998), Simulated response of the ocean carbon cycle to

anthropogenic climate warming, *Nature*, *393*, 245–249.

Schneider, B., R. Schlitzer, G. Fischer, and E. M. Nöthig (2003), Depth-dependent elemental compositions of particulate organic matter (pom) in the ocean, *Global Biogeochemical Cycles*, *17*, 1032.

Volk, T., and M. I. Hoffert (1985), Ocean carbon pumps: analysis of relative strengths and efficiencies in ocean-driven atmospheric co_2, in *The carbon cycle and atmospheric CO_2: Natural variations Archean to Present*, edited by E. T. Sundquist and W. S. Broecker, pp. 99–110, AGU, Washington D.C.

Zehr, J. P., and B. P. Ward (2002), Nitrogen cycling in the ocean: New perspectives on processes and paradigms, *Applied and Environmental Microbiology*, *68*, 1015–1024.

Figure 1. A schematic depiction of the PINC model; the model organisms need to take up DIC (X_C) together with light to form C-reserve (X_{EC}), while no light is needed for the uptake of DIN (X_N) into N-reserve (X_{EN}). The outflow from both reserves is combined in a fixed stoichiometry into a catabolic flux $\dot{J}_{V,C}$ that is used for the maintenance and growth of the structure (X_V). The dead organic material is divided into N-detritus (X_{DN}) and C-detritus (X_{DC}) which remineralise into DIN and DIC respectively.

Figure 2. Vector plot of the initial horizontal velocity distribution of the eddy (at 100 m depth). Maximum horizontal velocities are about 0.1 ms^{-1}.

Figure 3. Vertical velocity as a function of time at grid-point [0.5N,0.5M,L-1]; the crosses indicate the times at which the horizontal cross-sections have been taken.

Figure 4. Horizontal patterns at 20 m depth after 3.6 days. (a) Cross-section of the vertical velocity distribution; white indicates upwelling, black downwelling and maximum amplitudes are 6.5×10^{-3} ms^{-1}. (b) Cross-section of the nutrient distribution; white indicates high concentration, black low concentration, min. conc. 0.15 μM, max. conc. 23.5 μM. (c) Cross-section of the structural volume distribution; min. 0.002 μM, max. 1.1 μM.

Figure 5. Horizontal patterns at 20 m depth after 7.2 days. (a) Cross-section of the vertical velocity distribution; white indicates upwelling, black downwelling and maximum amplitudes are 1.6×10^{-3} ms^{-1}. (b) Cross-section of the nutrient distribution; white indicates high concentration, black low concentration, min. conc. 1.5 μM, max. conc. 30.5 μM. (c) Cross-section of the structural volume distribution; min. 0.001 μM, max. 1.6 μM.

Figure 6. Horizontal patterns at 20 m depth after 7.2 days. (a) Cross-section of the vertical velocity distribution; white indicates upwelling, black downwelling and maximum amplitudes are 0.6×10^{-3} ms^{-1}. (b) Cross-section of the nutrient distribution; white indicates high concentration, black low concentration, min. conc. 1.7 μM, max. conc. 23.4 μM. (c) Cross-section of the structural volume distribution; min. 0.06 μM, max. 3.5 μM.

Figure 7. (a) Horizontally averaged C:N ratio as a function of depth at different times. (b) Horizontally averaged X_N concentration as a function of depth at different times. (c) Horizontally averaged X_V concentration as a function of depth at different times.

Figure 8. Comparison between $< X_V >< \dot{j}_{E_N,A} >$ and $< X_V \dot{j}_{E_N,A} >$ as a function of depth after 7.2 days

Appendix A: PINC model formulation

The dynamics of the PINC model is governed by the following equations:

$$
\begin{aligned}
\frac{dX_C}{dt} &= F_1 = X_V(-\dot{j}_{E_C,A_A} + (y_{E_C,V} - 1)\dot{j}_{V,C_A} + (y_{DV,V} - 1)\dot{j}_{V,C_H} + \dot{k}_M) \\
\frac{dX_N}{dt} &= F_2 = X_V(-\dot{j}_{E_N,A} + (y_{E_N,V} - n_{NV})\dot{j}_{V,C_A} + n_{NV}(y_{DV,V} - 1)\dot{j}_{V,C_H} \\
&+ n_{NV}\dot{k}_M + (1-\kappa)\dot{j}_{E_N,R} + \frac{X_{E_N}}{X_V}\dot{j}_{V,H}) \\
\frac{dX_V}{dt} &= F_3 = X_V(\dot{j}_{V,G} - \dot{j}_{V,H}) \\
\frac{dX_{EC}}{dt} &= F_4 = X_V(\dot{j}_{E_C,A_A} + \dot{j}_{E_C,A_H} - \dot{j}_{E_C,C} + \kappa\dot{j}_{E_C,R} - \frac{X_{E_C}}{X_V}\dot{j}_{V,H})) \\
\frac{dX_{EN}}{dt} &= F_5 = X_V(\dot{j}_{E_N,A} + \dot{j}_{E_N,C} + \kappa\dot{j}_{E_N,R} - \frac{X_{E_N}}{X_V}\dot{j}_{V,H}) \\
\frac{dX_{DOC}}{dt} &= F_6 = X_V(-\dot{j}_{E_C,A_H} + (1-\kappa)\dot{j}_{E_C,R} + \frac{X_{E_C}}{X_V}\dot{j}_{V,H})) \\
\frac{dX_{DV}}{dt} &= F_7 = X_V(-y_{DV,V}\dot{j}_{V,C_H} + \dot{j}_{V,H})
\end{aligned}
$$

The various fluxes are given by:

$$
\begin{aligned}
\dot{j}_{V,C} &= \dot{j}_{V,C_A} + \dot{j}_{V,C_H} \\
\dot{j}_{V,G} &= \dot{j}_{V,C} - \dot{k}_M \\
\dot{j}_{V,C_Am} &= ((y_{E_C,V}/(\dot{j}_{E_C,Am_A} + \dot{j}_{E_C,Am_H}) + y_{E_N,V}/\dot{j}_{EN,A_m} \\
&- ((\dot{j}_{E_C,Am_A} + \dot{j}_{E_C,Am_H})/y_{E_C,V} + \dot{j}_{E_N,Am}/y_{E_N,V})^{-1})^{-1} \\
\dot{j}_{V,H} &= \dot{h}\frac{y_{E_C,V}\dot{j}_{V,C_A} + y_{DV,V}\dot{j}_{V,C_H}}{y_{E_C,V}\dot{j}_{V,C_Am} + \dot{j}_{DV,A_Hm}} \\
\dot{j}_{E_C,A_A} &= \frac{\dot{j}_{EC,Am_A}}{1 + \frac{K_C}{X_C} + \frac{J_{L,FK}}{J_{L,F}} - (\frac{X_C}{K_C} + \frac{J_{L,F}}{J_{L,FK}})^{-1}} \\
\dot{j}_{E_C,A_H} &= \frac{\dot{j}_{E_C,Am_H}}{1 + \frac{K_{DOC}}{X_{DOC}}} \\
\dot{j}_{E_C,C} &= (\dot{k}_E - \dot{j}_{V,G})\frac{X_{E_C}}{X_V} \\
\dot{j}_{E_N,A} &= \frac{\dot{j}_{E_N,Am}}{1 + \frac{K_N}{X_N}} \\
\dot{j}_{E_N,C} &= (\dot{k}_E - \dot{j}_{V,G})\frac{X_{E_N}}{X_V} \\
\dot{j}_{V,C_A} &= (\frac{y_{E_C,V}}{\dot{j}_{E_C,C}} + \frac{y_{E_N,V}}{\dot{j}_{E_N,C}} - (\frac{\dot{j}_{E_C,C}}{y_{E_C,V}} + \frac{\dot{j}_{E_N,C}}{y_{E_N,V}})^{-1})^{-1} \\
\dot{j}_{E_C,R} &= \dot{j}_{E_C,C} - y_{E_C,V}\dot{j}_{V,C_A} \\
\dot{j}_{E_N,R} &= \dot{j}_{E_N,C} - y_{E_N,V}\dot{j}_{V,C_A} \\
\dot{j}_{V,C_H} &= \frac{\dot{j}_{DV,Am}}{y_{DV,V}(1 + \frac{K_{DV}}{X_{DV}})}
\end{aligned}
$$

The standard parameters of the PINC model are:

Parameter	Interpretation	Dimension	Value
n_{NV}	N-content of structure	mol N/mol C	0.1
$\dot{j}_{EC,AmA}$	max. C uptake	d^{-1}	2.5
K_C	sat. const. C uptake	μM C	500
$\dot{J}_{L,FK}$	sat. light flux	M/s	25
$\dot{J}_{L,F}$	light flux	M/s	50
$\dot{j}_{EC,AmH}$	max. DOC uptake	d^{-1}	4.0
K_{DOC}	sat. const. DOC uptake	μM C	5.0
$\dot{j}_{EN,Am}$	max. N uptake	mol N/(mol C * d)	0.25
K_N	sat. comst. N uptake	μM N	0.1
$\dot{j}_{DV,Am}$	max. DV uptake	d^{-1}	5.0
$y_{DV,V}$	yield DV uptake	–	4.0
K_{DV}	sat. const. DV uptake	μM C	500
$y_{EC,V}$	yield C reserve	–	1.5
$y_{EN,V}$	yield N reserve	mol N/mol C	0.15
$\dot{k}_E$	reserve turnover	d^{-1}	4.0
$\dot{k}_M$	maintenance rate	d^{-1}	0.1
$\dot{h}$	hazard rate	d^{-1}	0.1
κ	kappa	–	0.9

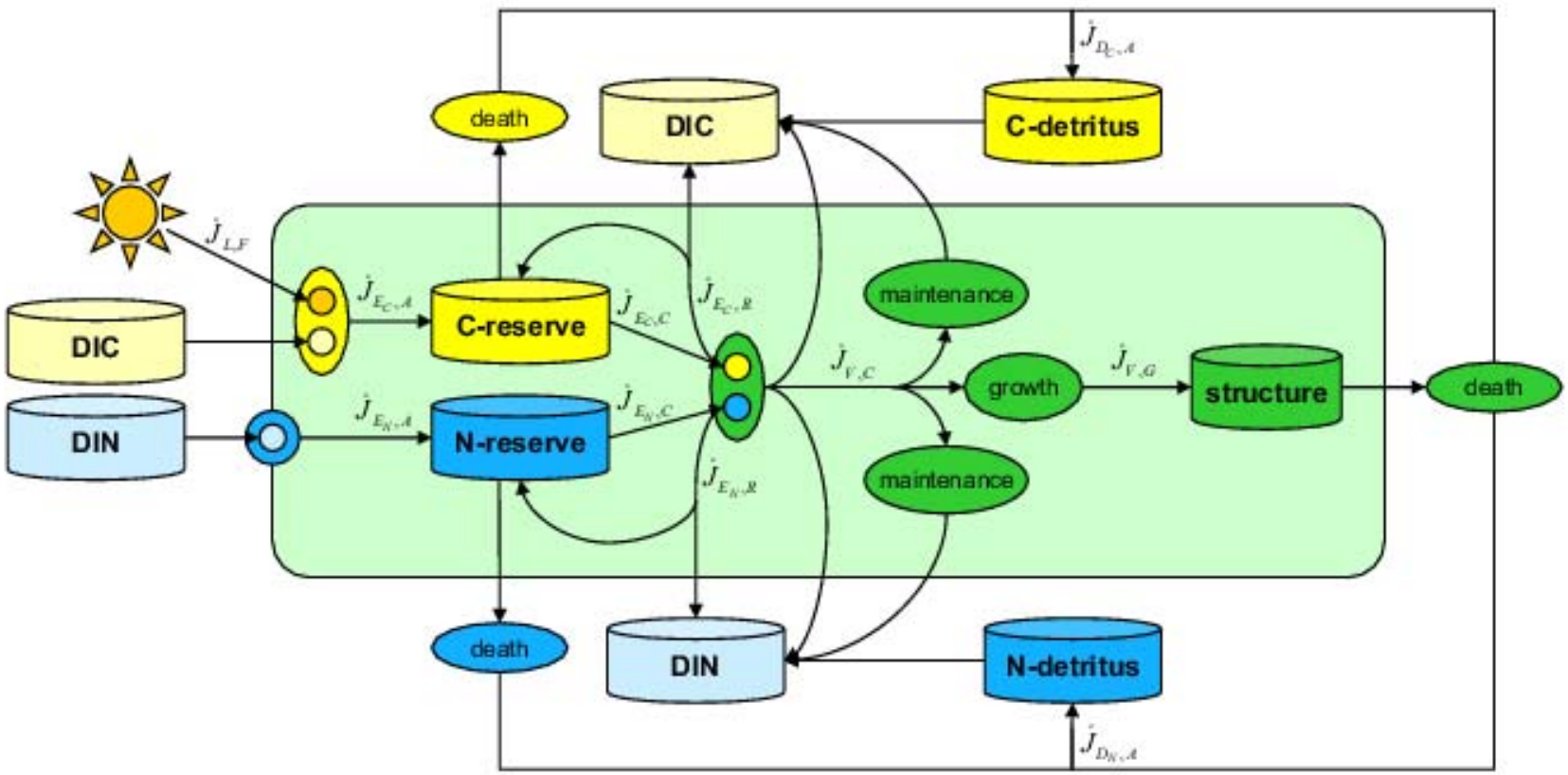
death
DIC
C-detritus
DIC
C-reserve
maintenance
growth
structure
death
DIN
N-reserve
maintenance
death
DIN
N-detritus

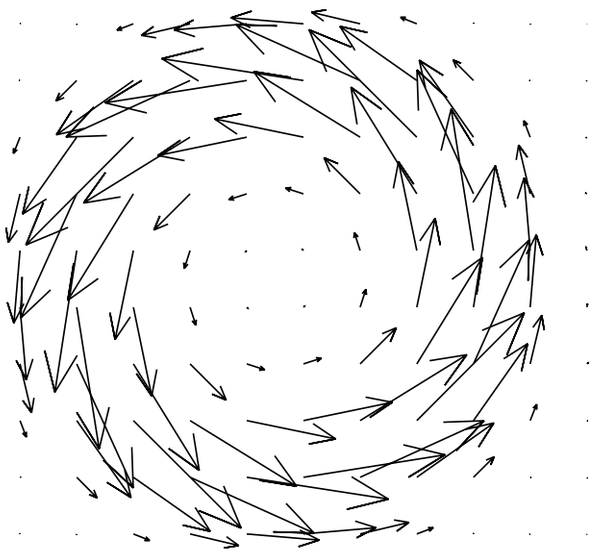

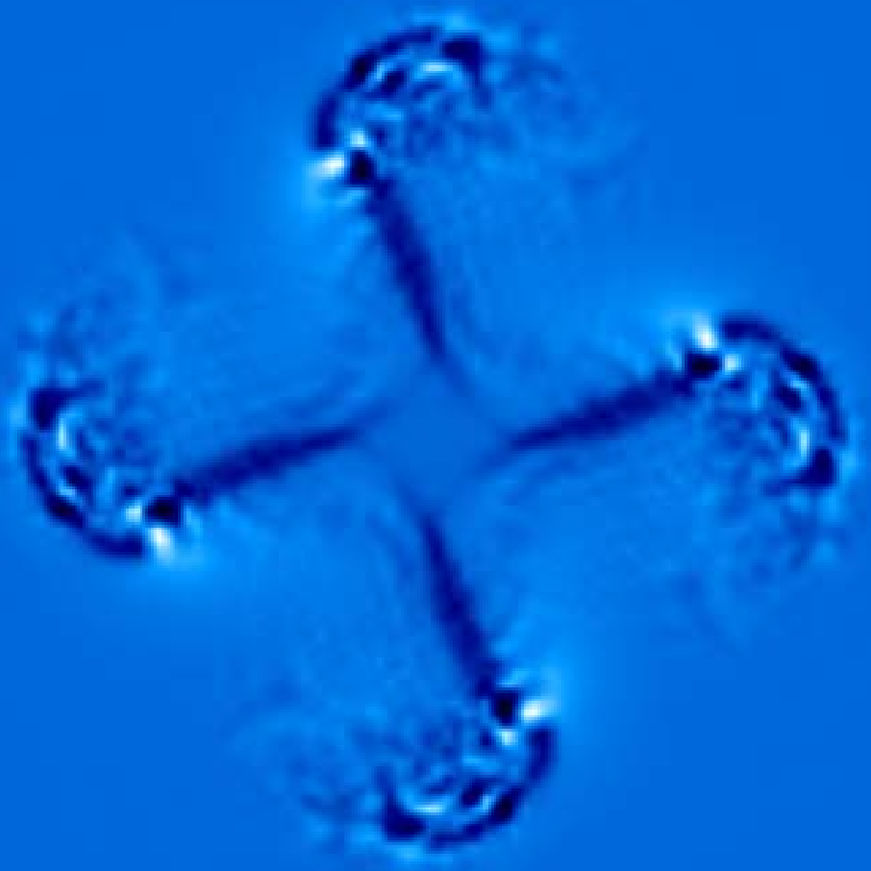

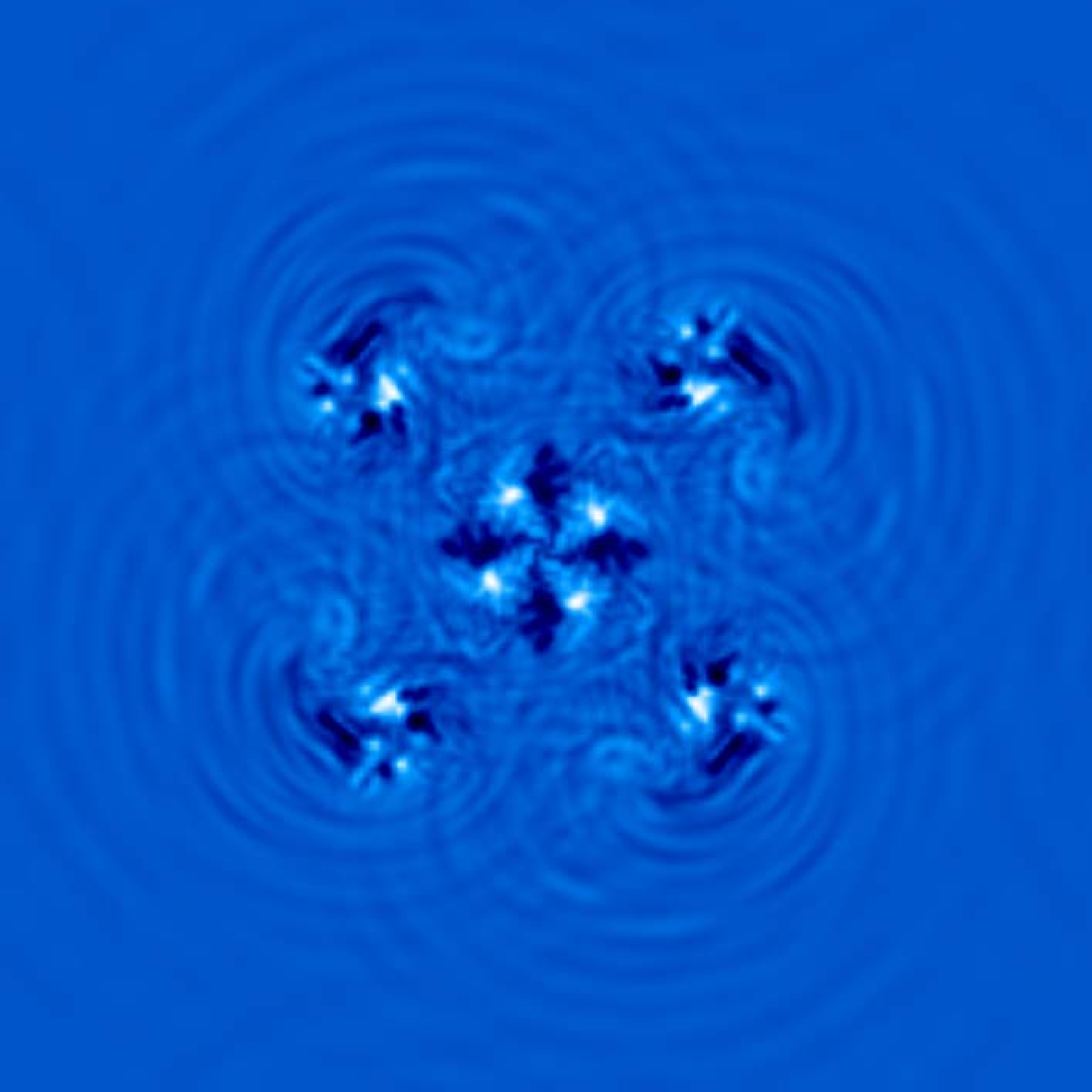

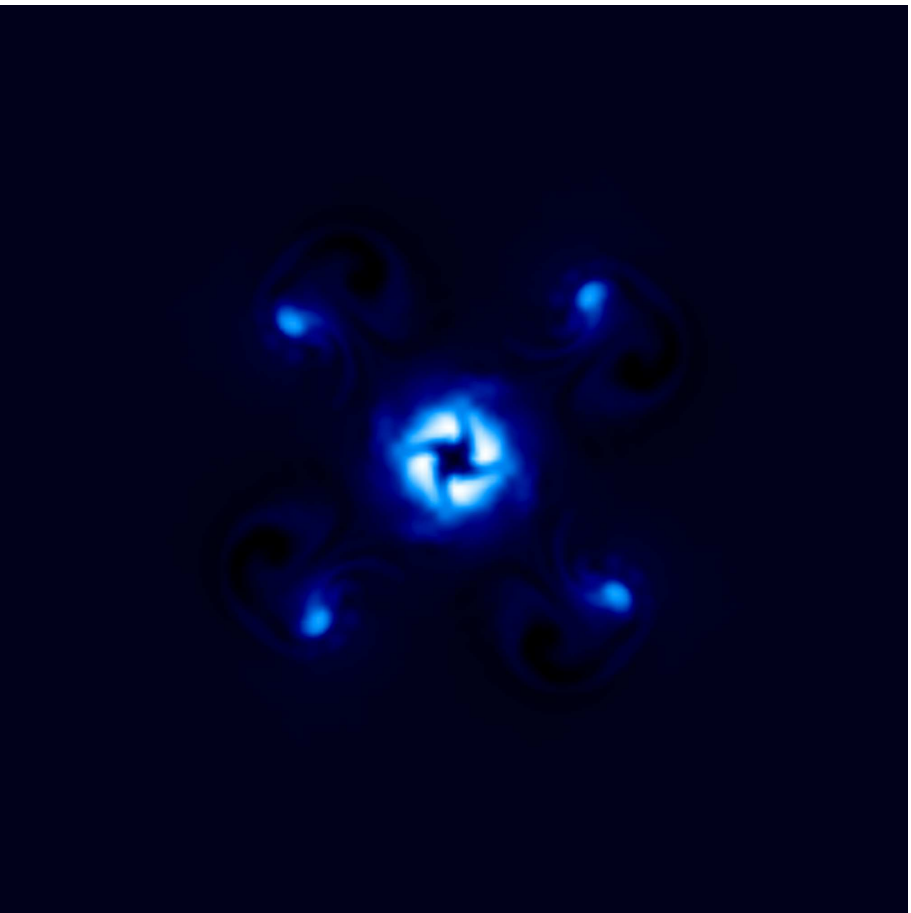

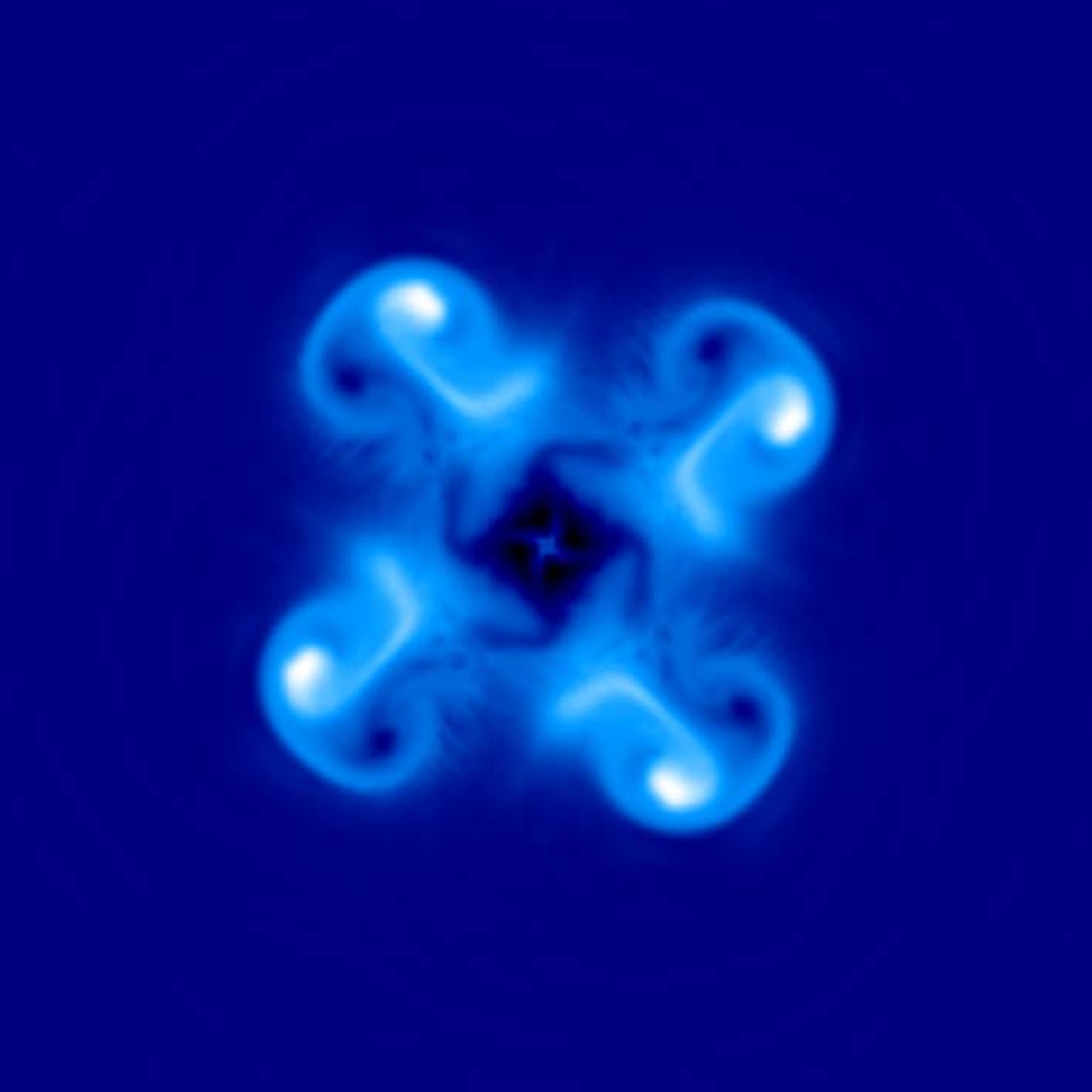

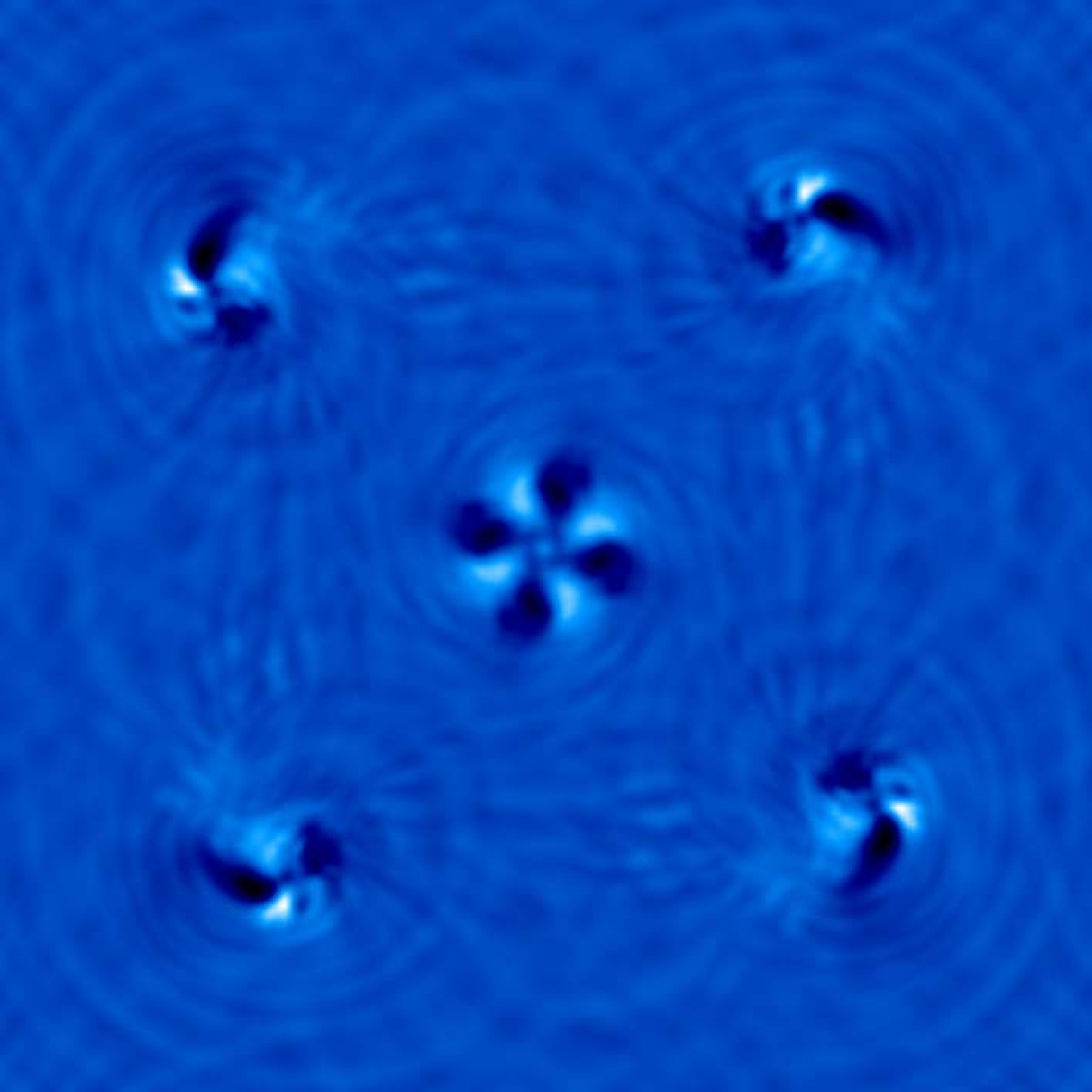

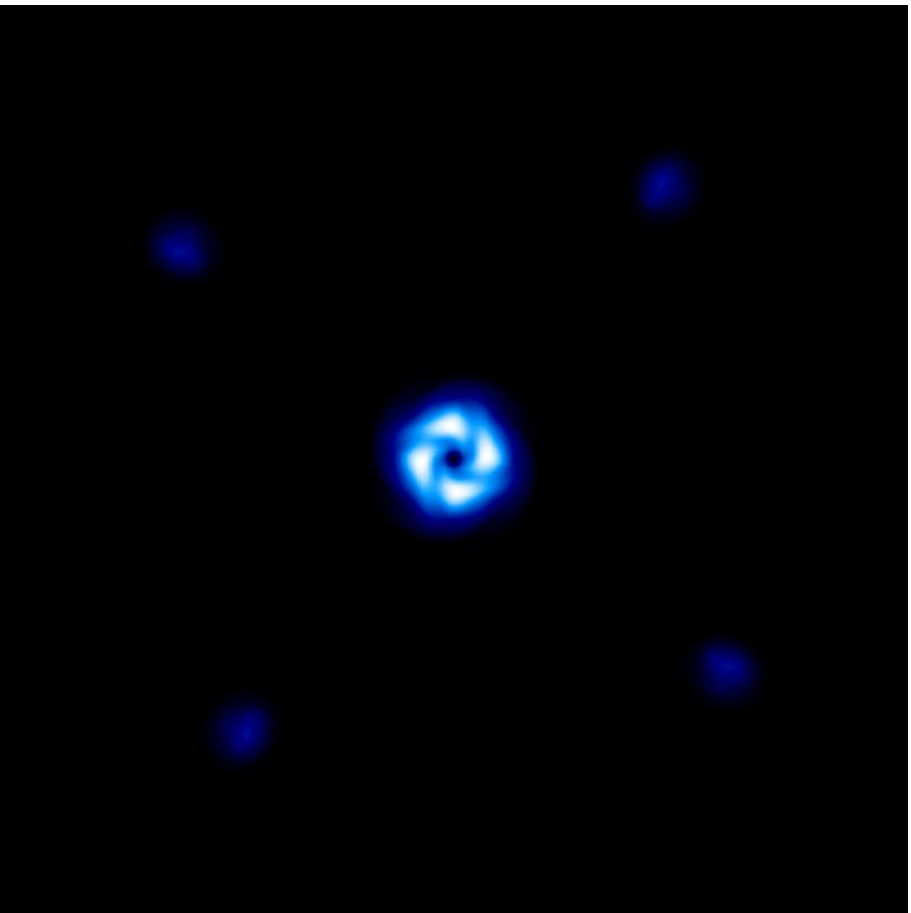

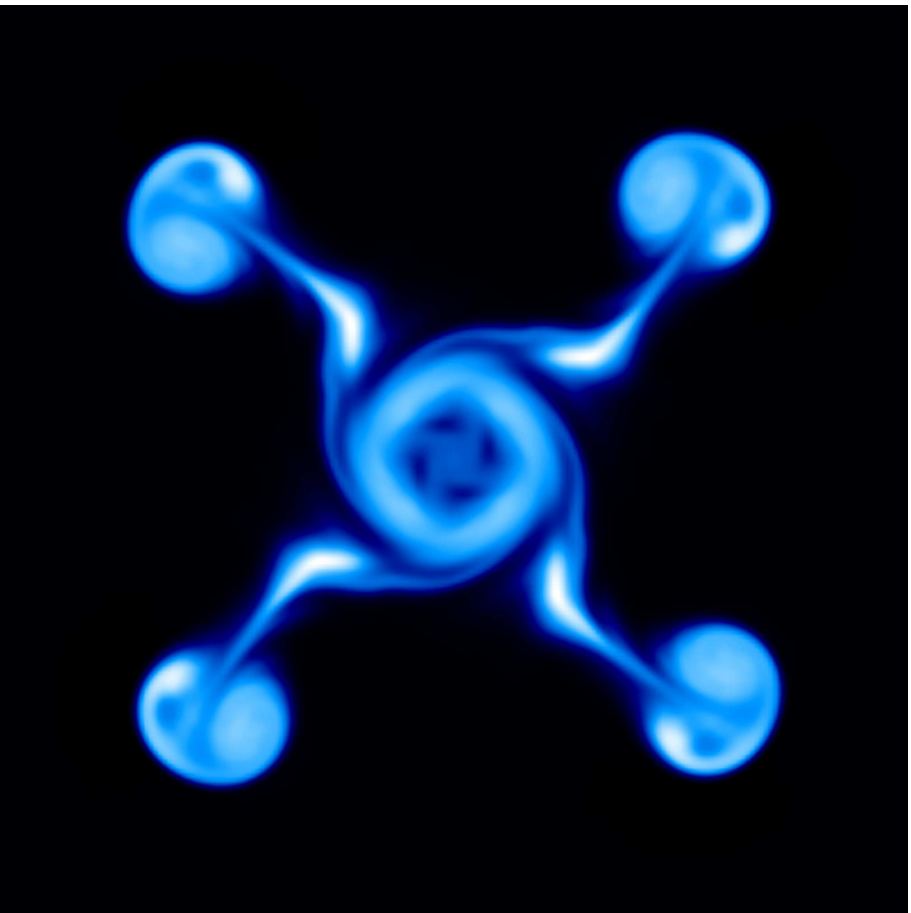

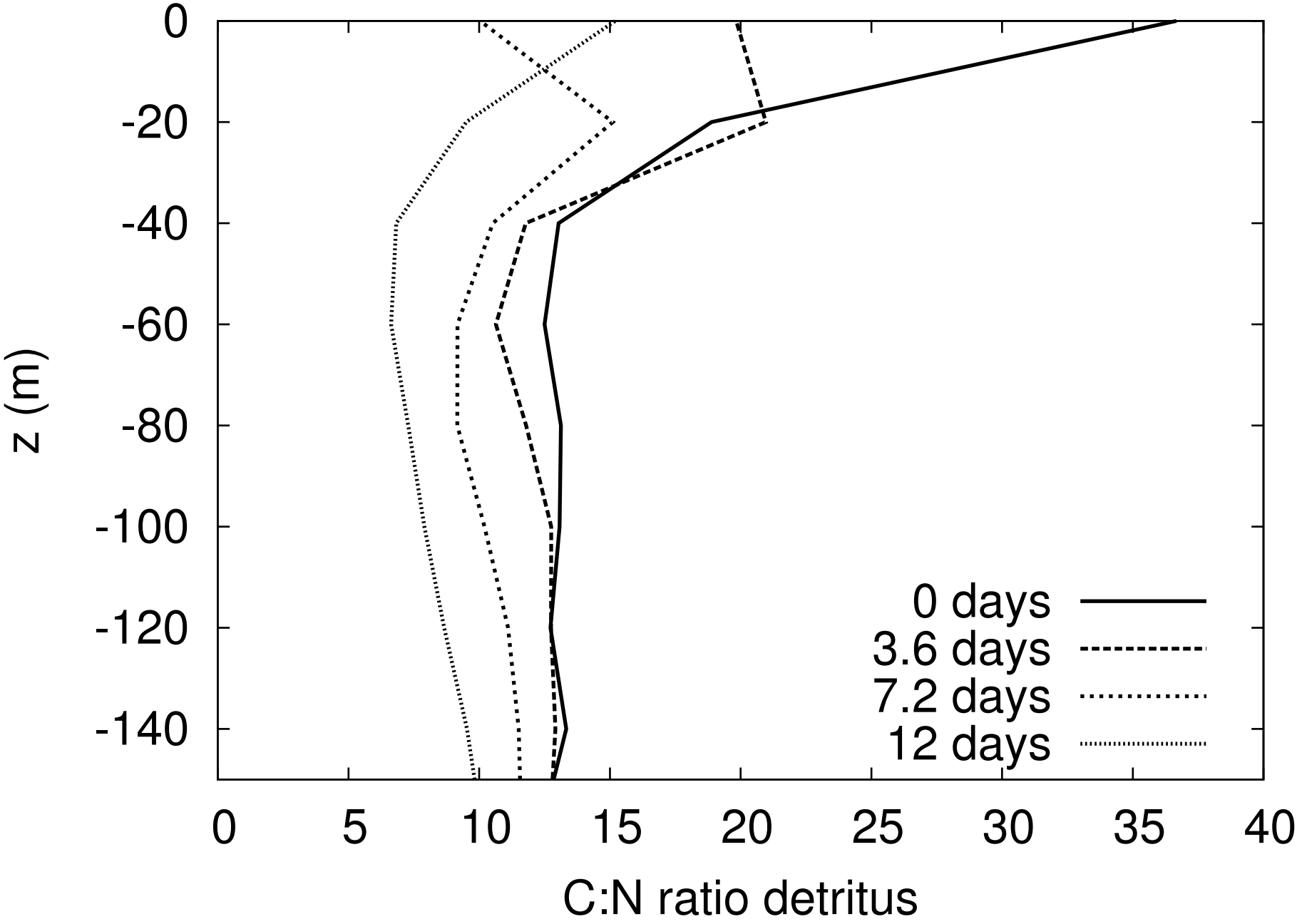
0
-20
-40
-60
-80
-100
-120
-140
z (m)
0
5
10
15
20
25
30
35
40
C:N ratio detritus
0 days
3.6 days
7.2 days
12 days

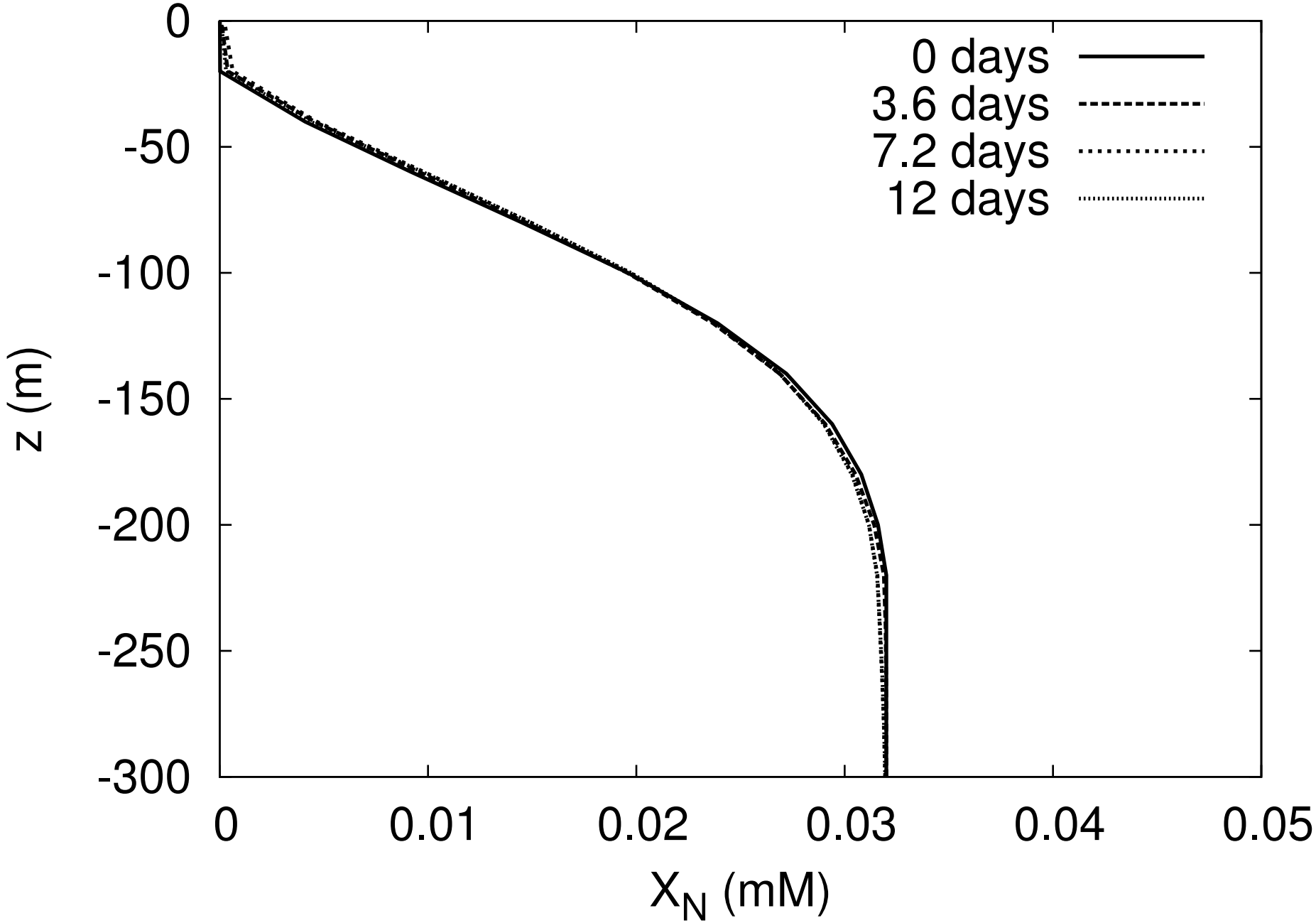
0
-50
-100
-150
-200
-250
-300
z (m)
0
0.01
0.02
0.03
0.04
0.05
X_N (mM)
0 days
3.6 days
7.2 days
12 days

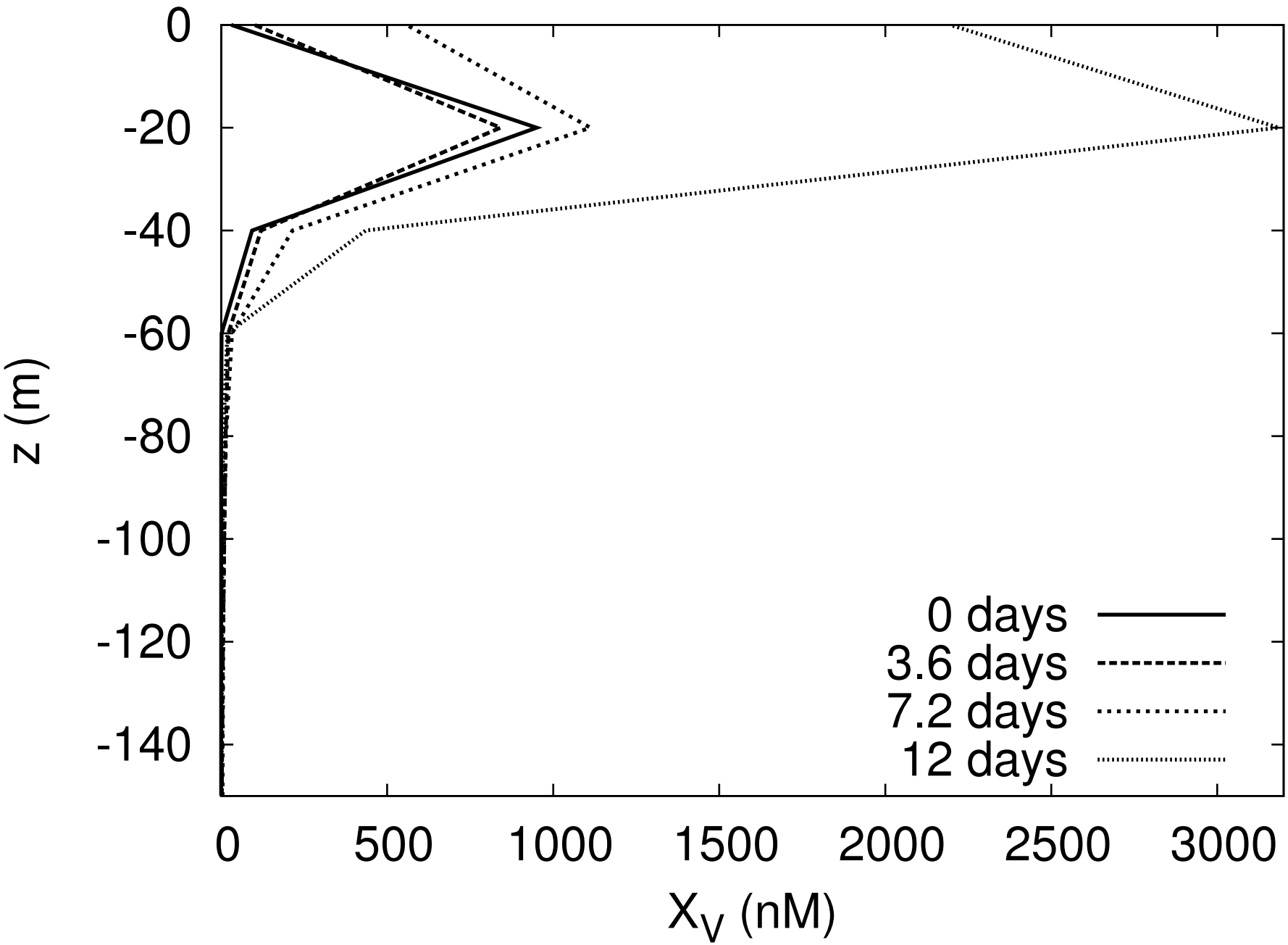
0
-20
-40
-60
-80
-100
-120
-140
z (m)
0
500
1000
1500
2000
2500
3000
X_V (nM)
0 days
3.6 days
7.2 days
12 days

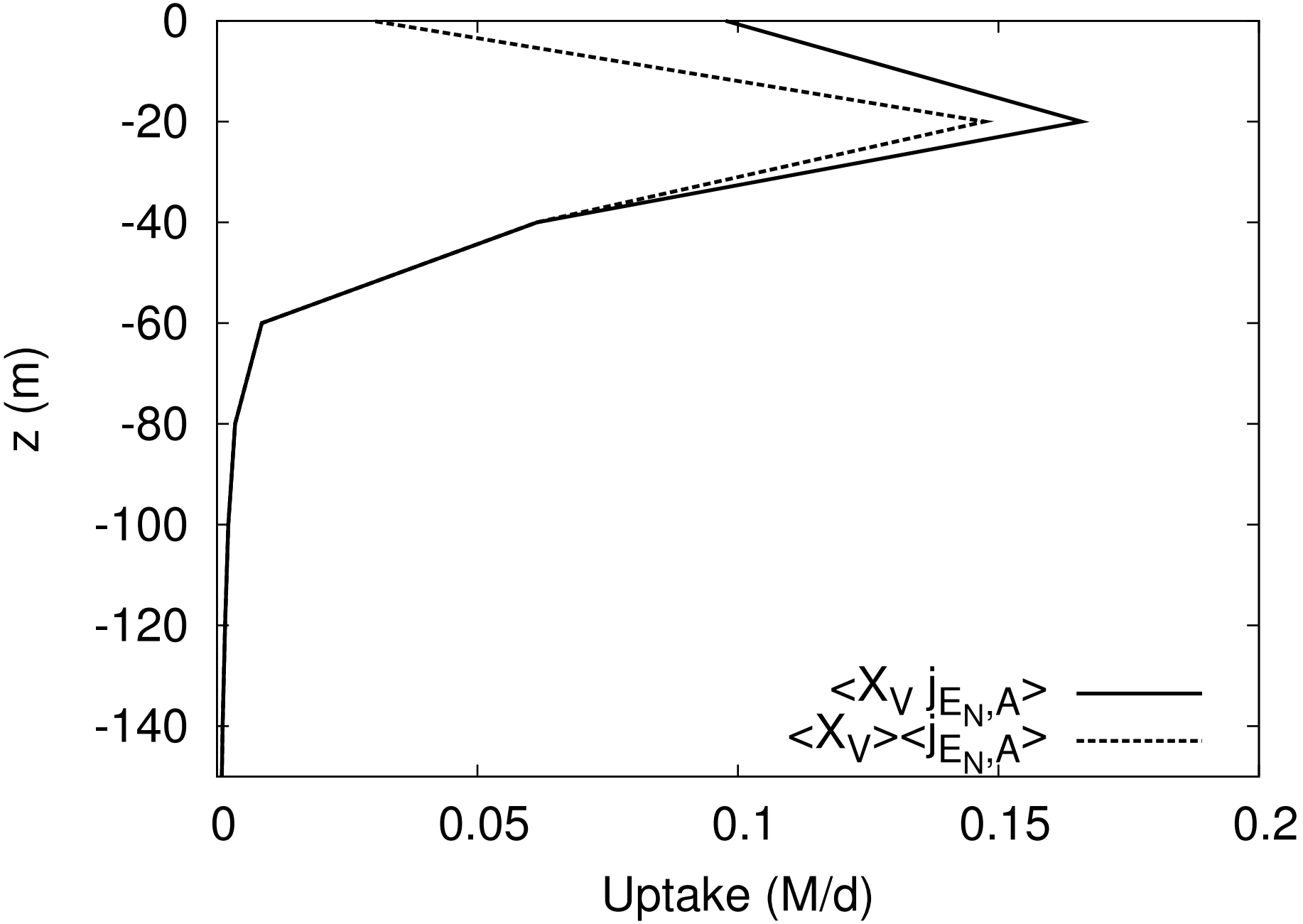
0
-20
-40
-60
-80
-100
-120
-140
z (m)
0
0.05
0.1
0.15
0.2
Uptake (M/d)
<X_V j_E_N,A>
<X_V><j_E_N,A>